Numerical and Field Tests Investigation of The Damage Distribution Under Blast Load

Magreth Dotto[1] and Yashar Pourrahimian[2]

[1,2] School of Mining and Petroleum Engineering, University of Alberta, Edmonton, Canada

ABSTRACT

In rock blasting, the intact rock properties and presence of structures affect the intensity and distribution of fractures in the rock mass. The study conducted from the field blast and numerical simulation using the Riedel–Hiermaier–Thoma (RHT) material model in LS-DYNA shows that structures do not necessarily halt the fracturing of the rock mass. Depending on the geometry and mechanical properties, the extent of damage can either be developed or arrested through structures. Structures' material properties and location relative to the blasthole, free face, and the pit wall influence the size and distribution of the fractures on the bench and the formation of the pit wall. Results comparison to the field measurements show general consistency in stress wave pressure and peak particle velocity attenuations, fracture distribution, and formation of the pit wall.

1. Introduction

Drilling and blasting is a controlled rock fracturing process using explosives that are extensively used in mining and civil works. In mining, blasting aims at achieving the average size and size distribution that safeguards the efficiency of the downstream processes of excavation, crushing, and milling while conserving the integrity of the remaining structures and mitigating adverse outcomes such as excessive ground vibration, fly rocks, air blasts, and over breaks. To achieve optimum results, it is important to understand the influence of physical and mechanical properties of the rock mass, the interaction between explosive energy and the rock mass, and rock fracture mechanisms [1, 2].

Rock fracturing by explosives is a rapid process, a combination of the action of higher shock waves and gas pressure from the explosion products in a blasthole. Shock waves cause pulverization around the blasthole and initiate cracks; explosion gases wedge into the cracks and extend them. The pulverized zone around the blasthole is commonly referred to as the crushed zone (CZ) and the tensile cracks dominate the fractured zone (FZ). The crushed zone is dominantly formed when the shockwaves exceed the dynamic compressive strength of the rock and as the stress wave propagates and the rock yields the fractured zone is formed when the stress wave exceeds the dynamic tensile strength of the rock [3-5]. Spalling is formed from the wave reflection at the free face when the reflected wave exceeds the rock's tensile strength [6]. These three are the significant damage zones in blast-induced rock fragmentation for mining processes.

Formation of damage zones varies significantly depending on the type and strength of the explosives and properties of the rock mass both the intact and structural properties. The impedance difference between the host rock and the structures' materials influences stress wave transmission across

ISBN: 978-1-55195-520-9

structures [2, 7]. Due to the complexity of studying the blasting process and the influence of structural properties on crack propagation and explosive energy distribution in the field blasts, numerical simulation has been used reliably to offer insight from the reconstructed field scenarios [8]. Numerical simulations have been used to understand the influence of various structural properties such as the structure's stiffness, yield strength, orientation, continuity, location, and fracture frequency on blast outcomes [1, 2, 9-11]. These studies concluded that structures alter the distribution and propagation of stress waves and fractures, hence fragmentation distribution and the extent of damage zones around the blasthole.

Analysis of rock mass in numerical modelling is usually limited to a regular structure or set of structures in a two-dimensional (2D) rock model which is simple and practical. The rock mass comprises the intact rock and a combination of several structures like faults, contacts, dykes, and joints. The analysis of such a system is critical in understanding the fragmentation distribution in bench blasting. In this study, a 2D reconstruction is made in LS-DYNA using the scanline mapping data to analyze the effect of the combination of several structures on blast outcomes. A case study data is used to model the explosive, rock, and discontinuity properties. The accuracy of the simulation results is confirmed by the fragmentation analysis obtained. This study offers insight to blast engineers on the combined influence of structures as a guide to blast designs.

2. Case study description

2.1. Geology and Structural Properties

The study is based on data collected from New Luika Gold Mine, which Shanta Gold owns. The New Luika Gold Mine is located in the Songwe District of Southwestern Tanzania. Shanta Gold operates several open pits and underground mines in this area. Data collection was done in the Shamba pit. Shamba geology comprises granodiorite, granites, and quartzofeldspathic as host rocks. Gold mineralization is hosted in the dipping brittle to brittle-ductile deformational features (shear zones), always accompanied by quartz veins occurring at various scales; a metre scale robust veins to millimetre scale veinlets dispersed throughout shear zones. The mineralized quartz veins strike NE-SW and dip NW 40 to 50 degrees. Dyke intrusives which include dolerite, pegmatite, aplite, and alaskite are observed cross-cutting major lithologies and therefore thought to be younger than the host rocks. The diamond core logging from two boreholes shows the distribution of lithologies by depth as indicated in Figure 1 and the rocks' physical and mechanical properties are shown in Table 1 [12].

The mapping conducted on the eastern, southern, and northern pit walls indicates the distribution of structures, most of which are 5 to 50 mm wide joints, dipping at an average of 67 degrees. Other common features are faults, veins, shear zones, and rock contacts dipping at steep angles between 70 and 80 degrees; the width ranges from a few millimetres to 6.7 m for faults. Most structures are empty or filled with clay, quartz, or hematite. The mapped structures on the pit wall levels 960 and 950 in Figure 2 and*Figure* 3 show the major faults.

2.2. Explosives and Blast Design

Shanta Gold has contracts with African Explosives Limited (AEL) for explosives supply and blasting services. As a blasting agent, the company uses S135 base emulsion density of 1.33 to 1.35 g/cm3. The explosive is sensitized by Sodium nitrite solution from base density 1.33 to 1.25 g/cm^3 as the final cup density. Unlike ANFO and cartridge explosives, the emulsion is cap-insensitive, requiring a booster to initiate. Priming is achieved using surface detonators, a downline detonator, and a booster. An electric current does the shot initiation through an instantaneous electric detonator (IED). The shock wave from its detonation triggers the trunk line initiation, from which the surface detonators are initiated and detonate at their assigned sequence. Surface detonators have shot period

delays (SPD) ranging from 17 to 75 ms. After being initiated, the surface detonator sends a signal to a downline detonator, and 500ms shock tubes are used. The shock tube triggers the booster, and the explosive column is finally initiated from the bottom up.

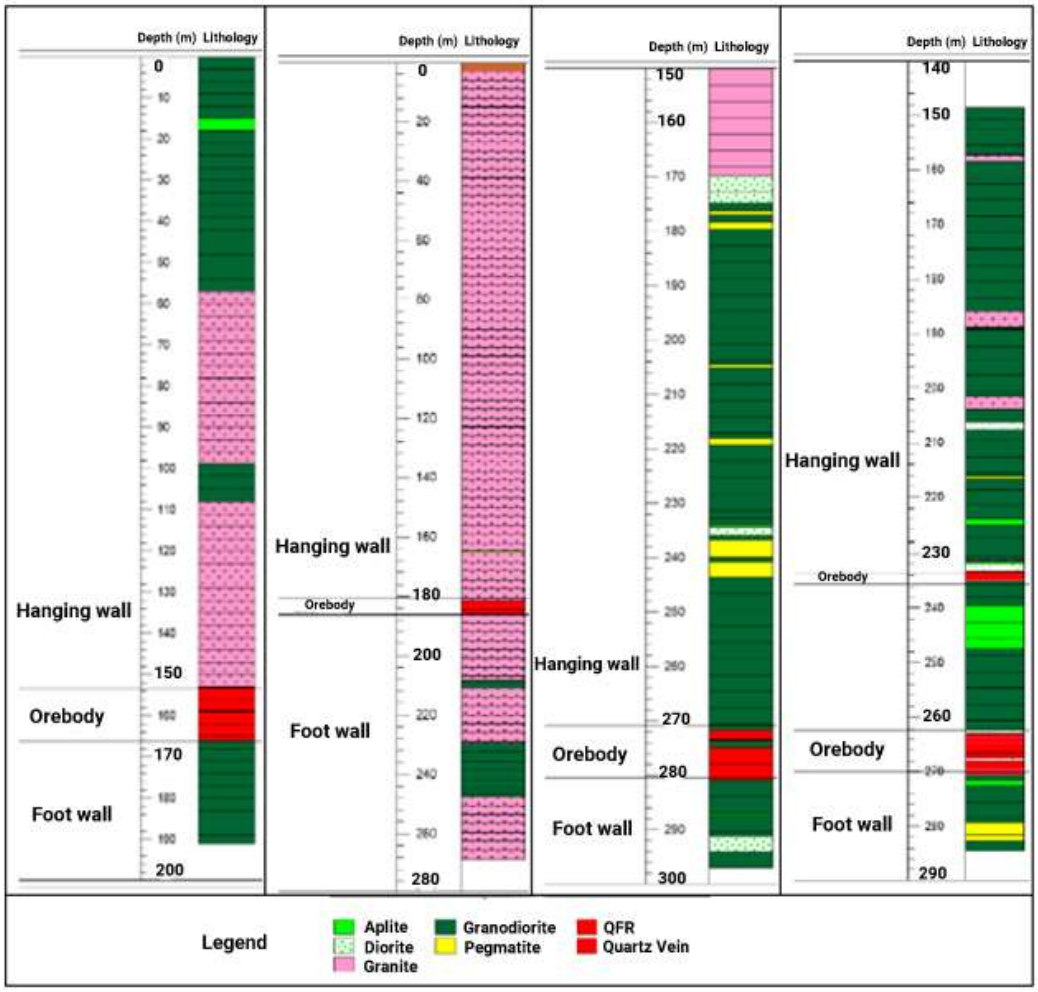

Figure 1: Lithology distribution in New Luika Mine after Hanekom, et al. [12].

Table 1: Rocks' physical and mechanical properties.

Rock type	Rock code	UCS(σ_c), MPa	Young Modulus (E), GPa	Poisson ratio	Rock density (ρ_r), kg/m^3	P-wave velocity (V_p), m/s	Tensile strength (σ_t), MPa
Granite	GRN	286.72	61.93	0.31	2,698	4,791	29
Granodiorite	GDIO	284.70	72.05	0.33	2,831	5,045	28
Diorite	DIO	161.87	70.78	0.30	2,952	4,897	16
Aplite /Pegmatite	APL /PEG	229.05	68.00	0.38	2,622	5,093	23

Quartz vein/Quartz feldspar rock	QV /QFP	269.95	83.90	0.13	2,685	5,590	27

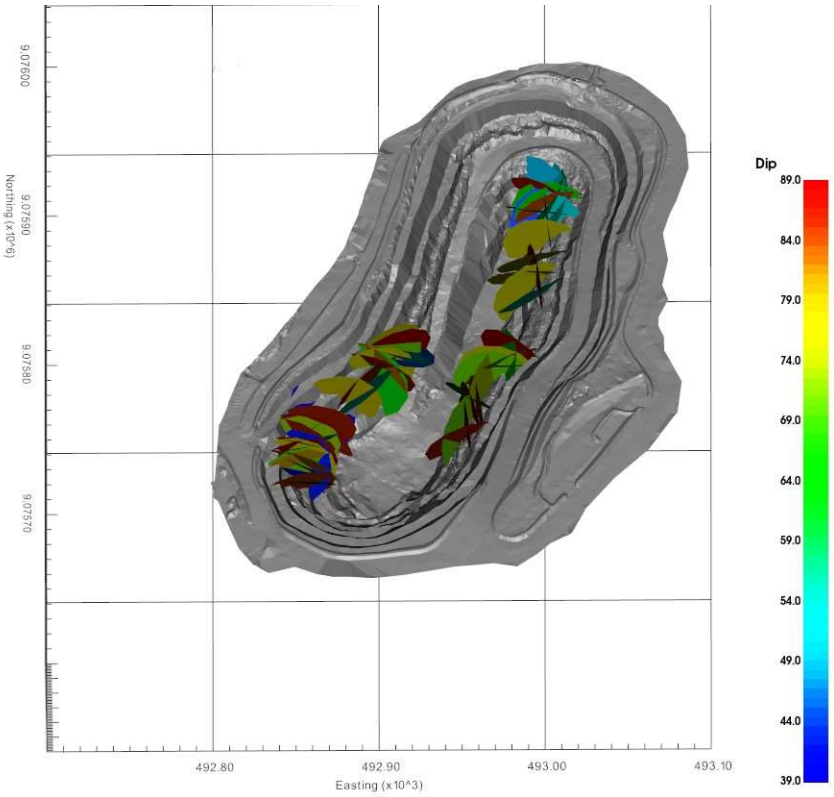

Figure 2: Mapped pit wall joints.

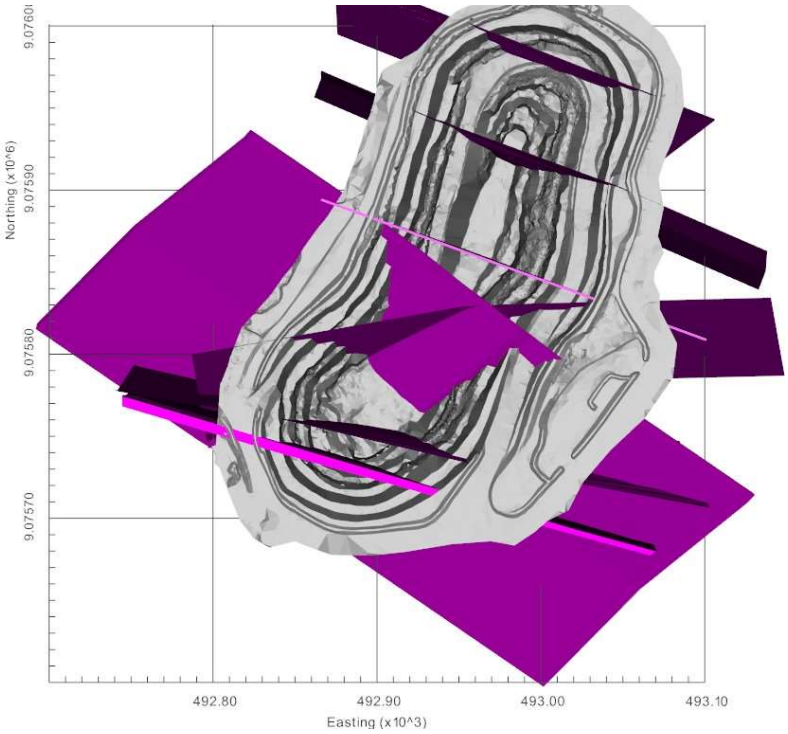

Figure 3: Mapped major faults.

Blast design is categorized into ore or waste shots. To prevent dilution in a narrow orebody, the 5 m bench height is used with 5.5 m blastholes, charged 2.6 m and 2.4 m stemming. For waste shots, 10 m benches are used with the burden, spacing, charging length, and stemming height of 3.7 m, 4.3 m, 6.7 m, and 3.4 m, respectively. The summary of explosive properties and blast design are shown in Table 2.

Table 2: Explosive and blast design parameters.

Explosive properties		**Blast design parameters**		
Explosive type	S135	Parameter (units)	Ore shot	Waste shot
Mixing	35% AN 65% Emulsion	Diameter (mm)	102	127
Max hole depth	40 m	Spacing (m)	3.2	4.3
Density (g/cm3)	1.00 to 1.25	Burden (m)	2.8	3.7
RWS at 100 MPa	111-115	Bench height (m)	5.4	10.1
RBS at 100 MPa	174-178	volume (m^3)	48.384	160.691
Ideal energy (MJ/kg)	2.5 – 2.7	Stemming (m)	2.6	3.4
VOD (m/s)	4500	Charging length (m)	2.8	6.7
Critical diameter (mm)	100	Charge per hole (kg)	28.60	106.09
Initiation	150 g booster and shock tube 500 ms 7 or12m long	Powder factor (kg/m^3)	0.59	0.66

3. Numerical modelling

3.1. Geometrical Design

The numerical model is constructed in LS-DYNA using the RHT model, which is widely used to simulate rock blasting. The model can successfully model the dynamic response of the rock mass and blast-induced damage [13-15]. Model construction in LS-DYNA is comprised of the geometrical design, the definition of the materials model, the interaction between different parts, and the definition of boundary conditions. Geometrical design is formed by the nodes, elements, and parts; in this study, the hexahedral elements with 8 nodes are used for all parts. Three parts, which represent the explosives, rock, and structures, are used. Explosive elements range from 3 to 6 mm, rock elements from 6 mm to 3 cm, and structures, unless limited by the structure's width are 3 cm. The model size follows the bench design; the description of the parameters is summarized in Table 3. The analysis uses two-dimensional (2D) models for the influence of material properties and orientations on the distribution of explosive energy and fractures as well as the formation of pit wall. All model scenarios are based on the mapping data for comparison with the field measurements.

Table 3: Summary of geometrical parameters.

Parameter	Value
Blasthole diamater (mm)	102
Burden (m)	2.8
Spacing (m)	3.2
Boundary conditions	
Free boundaries (free face)	West and top
Transmitting boundaries	East, North, South
Fixed movement	Along the depth

3.2. Material Models

The RHT model parameters are determined using the rock mechanical properties as shown in Table 4. The rock material as seen in Figure 1 comprises mainly granodiorite and granite rock types, which have similar properties. Granite properties are used to estimate RHT material parameters for the rock mass. More information on the estimation of model parameters can be found in the literature [2, 16-19].

Table 4: Granite RHT material model.

Parameter (unit)	Value	Parameter (unit)	Value
Density, RO (kg/m^3)	2698	Compressive strain rate exp, BETAC	0.026
Elastic shear modulus, SHEAR (GPa)	23.64	Tensile strain rate exp, BETAT	0.007
Unit factor, ONEMPA	0	Pressure influence on plastic flow in tension, PTF	0.001
Eroding plastic strain, EPSF	2	Compressive yield surface parameter, GC	0.53
Pore crush par , B0	1.22	Tensile yield surface parameter, GT	0.7
Pore crush par , B1	1.22	Shear modulus reduction factor, XI	0.5
Bulk modulus, T1 (GPa)	54.32	Damage parameter, D1	0.04
Failure surface parameter, A	1.6	Damage parameter, D2	1
Failure surface parameter, N	0.6	Minimum damage residual strain, EPM	0.015

Compressive strength, FC (MPa)	286.72	Residual surface parameter, AF	0.61
Relative shear strength, FS	0.18	Residual surface parameter, NF	1.6
Relative tensile strength, FT	0.1	Gruneisen gamma, GAMMA	0
Lode angle dependency factor, Q0	0.68	Hugoniot polynomial coefficient, A1 (GPa)	54.32
Lode angle factor, B	0.1015	Hugoniot polynomial coefficient, A2 (GPa)	76.05
Bulk modulus T2 (GPa)	0	Hugoniot polynomial coefficient, A3 (GPa)	28.25
Ref compressive strain rate, EOC	3×10^{-5}	Crush pressure, PEL (MPa)	191.15
Ref Tensile strain rate, EOT	3×10^{-6}	Compaction pressure, PCO (GPa)	6
Break compressive strain rate, EC	3×10^{25}	Porosity exponent, NP	3
Break tensile strain rate, ET	3×10^{25}	Initial porosity, ALPHA	1

Emulsion explosive S135 manufactured by AECI Mining Explosives is used for bench blasting. Explosive detonation is described by the high explosive burn material constructive model and the Jones-Wilkins-Lee (JWL) equation of state (OES). The parameters from the explosive properties in Table 2 and constants JWL EOS constants adopted from Hansson [20] are used to define material and EOS parameters as listed in Table 5.

Table 5: Material and JWL EOS parameters of S135 emulsion.

Explosive Type	Density (kg/m^3)	VOD (m/s)	Pcj (GPa)	A (GPa)	B (GPa)	R1	R2	ω	Eo (GPa)	vo
Emulsion (S135)	1,250	4,500	6.328	2.43	7.67	4.99	1.967	0.499	2.7	0

Structural properties are categorized as joints, quartz veins, and faults. Clay is modelled for joints infill material as plastic kinematics with properties defined in Table 6 [2]. Fault material (diorite) is modelled using RHT material models from the mechanical properties in Table 1, considering the weakening of its properties from shearing. Quartz veins are mostly intact and are modelled using the RHT material model using properties in Table 1.

Table 6: Clay-filled joints properties.

Density, (kg/m^3)	Young's Modulus, (GPa)	Poisson ratio,	Yield stress, (MPa)	Tangent Modulus, (GPa)	Hardening parameter	Failure strain
1,600	5	0.35	0.4	4	0	0.5

LS-DYNA makes it possible to model the interaction between the solid material with fluids. Rock and structures are modelled as Lagrangian parts while the explosive (explosion gases) are modelled as Arbitrary Lagrangian-Eulerian (ALE) parts. The coupled charge is adopted where the size of the charge diameter is the same as the blasthole diameter. Coupling between Lagrange and ALE parts is established using constrained Lagrange in solid with Lagrange parts as slaves and ALE parts as masters.

3.3. Model Validation and Verification

An intact rock model is constructed for granite using the parameters discussed in sections 3.1 and 3.2 above, and the simulation is run for 2.5 ms. Simulation results obtained are compared with the results obtained from the field measurements using the approach presented in Dotto et al. [21] for estimation of the size of damage zones. Esen et al. suggested that the size of the crushed zone is a function of borehole pressure, blasthole radius, and rock dynamic properties [4]. Using the data

collected on explosive and rock properties, the size of the crushed zone (CZ) is estimated to be 87.71 mm, which is 1.72 times the radius of the blasthole.

Fracture zone (FZ) is estimated from the peak particle velocity (PPV) monitoring using Forsyth (22) expression to determine the critical PPV of the stress wave that can induce fractures in a rock mass. PPV monitoring conducted in five (5) shots indicates the PPV attenuation in the rock mass described in Figure 4. From the PPV attenuation and the rock's dynamic tensile strength, the fracture zone's size is estimated to be 3.02 m. More information on the estimation of the crushed zone and fracture zone can be found in Dotto et al. [21].

Shot Number	Distance (m)	Mass per 8ms delay (kg)	SD ($m/kg^{0.5}$)	PVS, (mm/s)
SH_OB_955 _D04D05	117.4	125	10.15	26.07
SH_WB_960 _E04E05	180.7	336	7.19	23.75
SH_OB_950 _D07D08	38.7	117	5.56	36.03
SH_WB_950 _E05E06	744.7	236	34.74	3.26
SH_OB_955 _D04D05	117.4	52	12.47	14.56

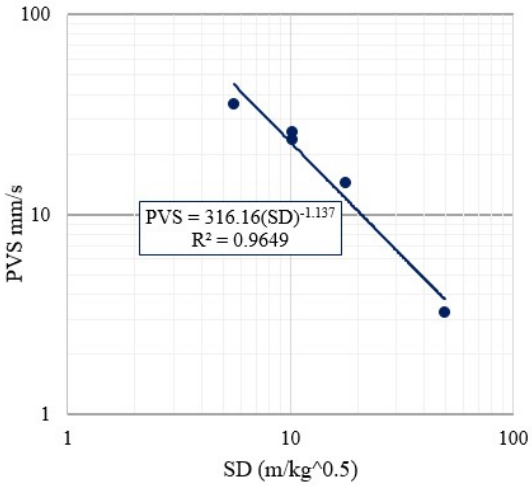

Figure 4: Peak particle velocity attenuation in the rock mass.

The simulation shows that after explosive detonation, higher pressure from the explosion products causes blasthole expansion from 51 mm to 68 mm. The crushed zone of 93.09 mm forms at 0.12 ms, and at the end of the simulation, the fractures extend to 3.1 m in the fractured zone as seen in Figure 5. Further cracking is seen on the free face side, which is caused by spalling from the stress wave reflection at the free face. Table 7 compares the results obtained from the simulation using the analytical approach by Dotto et al. [21]. From the comparison, the two approaches offer similar results with minor variations that can be due to the presence of structures in the rock mass from the field measurements that are not accounted for in the simulation. The simulation model is feasible since it performs as expected and offers comparable results.

Table 7: Results Comparison.

Approach	CZ radius (mm)	Pressure at the end of CZ (MPa)	PPV at end of CZ (m/s)	FZ radius (m)	PPV at the end of FZ (m/s)
Dotto et al. [21]	87.71	1,397	90.25	3.02	1.74
Simulation	93.09	1,290	102.00	3.1	2.35

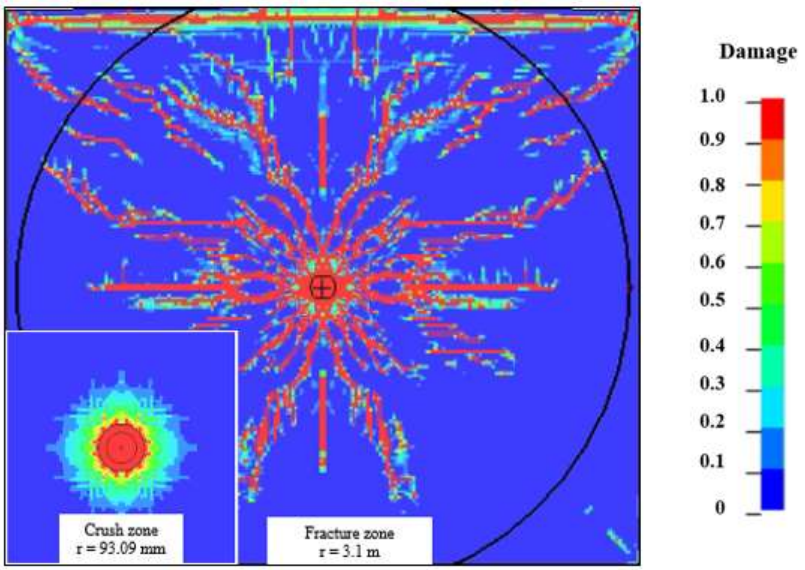

Figure 5: Simulated damage zone sizes.

4. Fracturing Analysis and Discussion

The analysis focuses on the ore shot SH_OB_955_D04D05, which in this study is termed shot 1. The design, firing direction, and material movement are shown in Figure 6(a) and (b). Centre lifting is applied due to the absence of a free face, where material movement is towards the centre. Centre lifting is usually discouraged due to the large number of movements in variable directions, which causes ore dilution. With centre lifting, higher and most variable vertical movements are observed in the control line (trunk line), and greater movements in the mid-bench cause higher dilution. Dilution can be minimized by moving the control line away from the boundaries of ore blocks.

4.1. Scenario 1-Two Intersecting Joint

Four interesting scenarios are re-created in LS-DYNA to explain the fragmentation and pit formation that were obtained in the field. The first scenario is the formation of oversize fragmentation and a hard dig muckpile in fragmentation analysis BF 30. The simulation model was created for the position of blasthole and structures as shown in Figure 7(a). Survey data shows that the fragmentation analysis was conducted on the opposite side of the intersected joints from the blasthole. From the fragmentation image taken from the muckpile and analysis done on wip-frag software in Figure 7(c) and (d), fragmentation on the incident side of the joint is fine while the opposite side is less fractured [23]. This is also observed in the re-created simulation results in Figure 7(e).

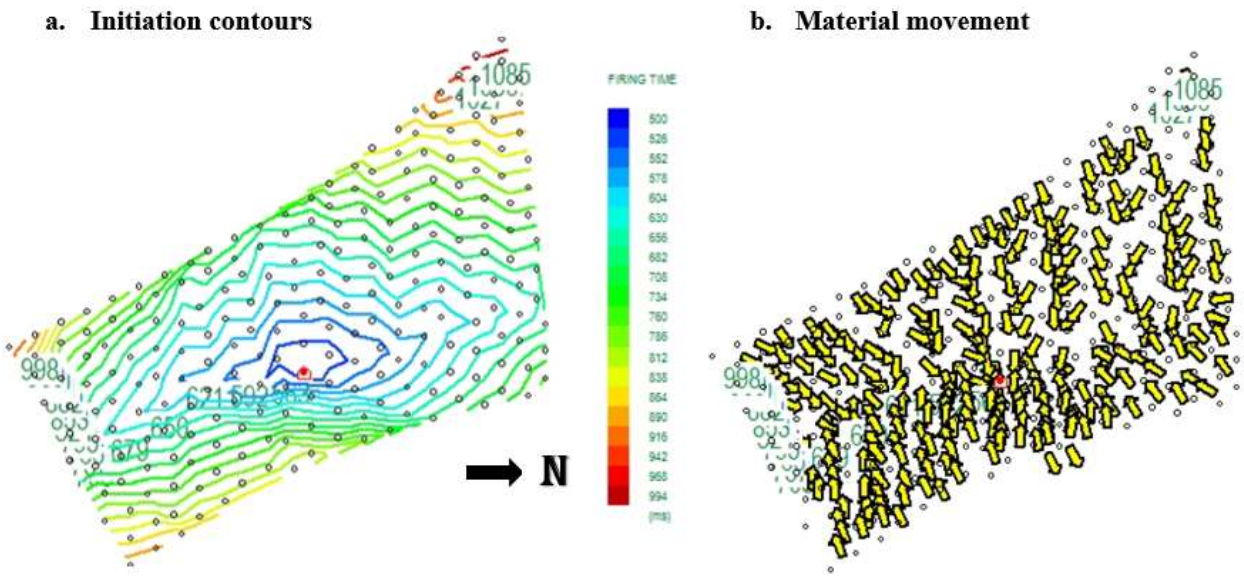

Figure 6: Shot initiation sequence and material movement.

a. Field mapping and survey

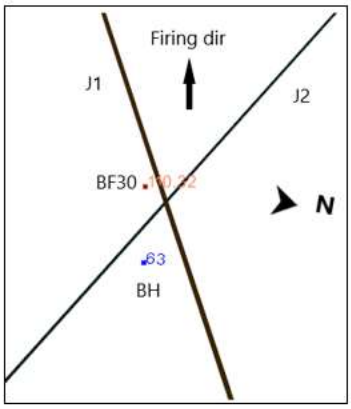

b. Joints properties

Structure	Joint 1 (J1)	Joint 2 (J2)
Dip (°)	80	60
Dip/strike direction (°)	160/250	290/20
Width (cm)	5	2
Infill	clay	clay
Firing direction	West	

c. Fragmentation image

d. Fragmentation analysis

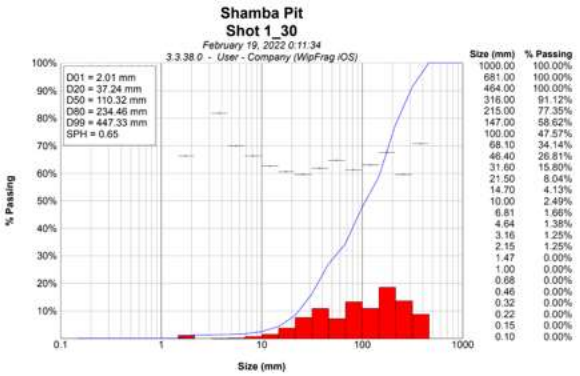

e. Scenario 1 simulation in 2D

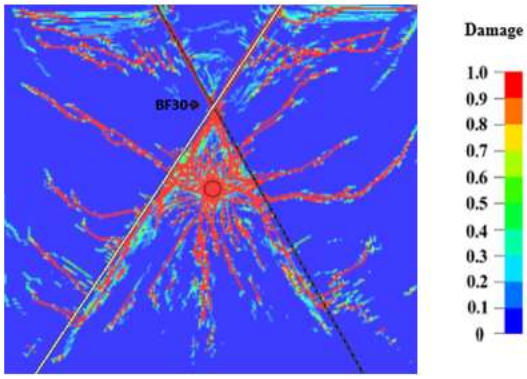

Figure 7: Scenario 1 Analysis.

The fragmentation image in Figure 7(c) also shows that the opposite side of the joint has minimal material movement, which can be due to the escape of explosion gasses through the interface between the rock and the joint. Simulation results show most of the stress wave energy is reflected at the interface, especially on the wider joint side. In addition to partial reflection, there is a re-direction stress wave when the two joints intersect, as described in Figure 8(a). That in addition to double reflection towards the free face, leaves the majority of the middle wedge on the free face uninterrupted as seen in Region 5 of Figure 8(b). Region 1 experiences better fragmentation if compared to Figure 5 (intact rock) by being on the incident side of the reflected stress wave. Fragmentation in regions 3 and 4 can be improved by adding extra blastholes on the opposite side of the joints.

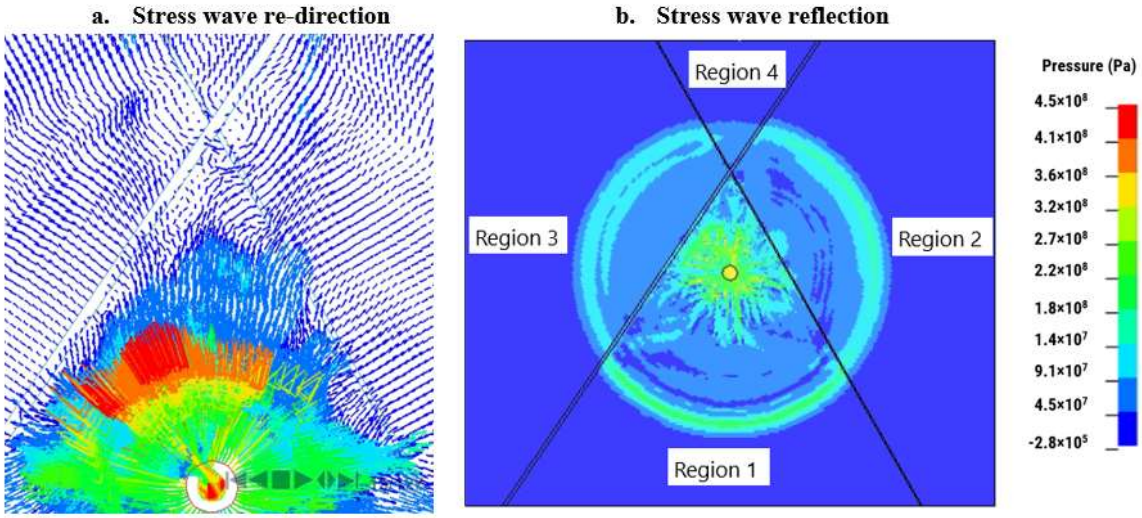

Figure 8: Energy reflection and re-direction at the joints.

4.2. Scenario 2-Fault on the Shot Boundary

The second scenario is the formation of oversize material with P50 and P100 of 0.54 m and 1.26 m, respectively, on the northern boundary of the shot. The fault is 0.97 m from the last blasthole on the shot boundary and is 1.5 m wide. The fault material is a mixture of diorite and granodiorite. The layout of the blasthole relative to the structure and fragmentation analysis point is shown in Figure 9(a), and the fragmentation image and its distribution are presented in Figure 9(c) and (d). The analysis suggests a mixture of smaller and bigger fragments with fragments less or equal to 0.4 m contributing only 40% of the muckpile. The remaining fragmentation ranges from 0.5 to 1.3 m.

From the recreation of the scenario in a numerical model, it is observed that the stress wave is reflected/attenuated as it crosses the interface between the rock and the fault (Figure 10(a)), causing more fracturing on the incident side, as seen in Figure 9(e). Fractures can still form on the fault because the material is weaker (softer) than the rock, although they are widely spaced due to an increase in rock strength caused by increased confinement when the stress wave crosses the second interface, as described in Figure 10(b). A combination of stress wave reflection on the free face and wave enhancement on the second interface forms fractures on the opposite side of the fault. The oversized fragmentation is caused by the spaced fractures on the fault and the quarter of the bench on the fault opposite the free face, which is almost uninterrupted. Since this was a shot interface, the oversized fragmentation could also be due to the escape of blast energy through the fractures formed by prior blast shots.

a. Field mapping and survey

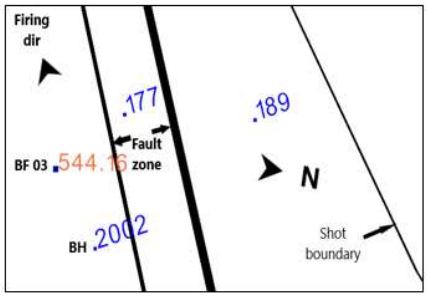

b. Fault properties

Structure	Fault
Dip (°)	75
Dip/strike direction (°)	22/112
Width (cm)	1500
Infill	Diorite
Firing direction	West

c. Fragmentation image

d. Fragmentation analysis

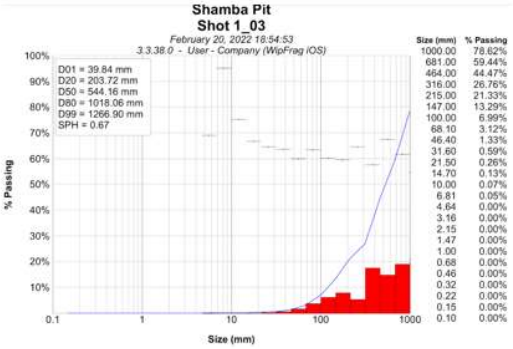

e. Scenario 2 simulation in 2D

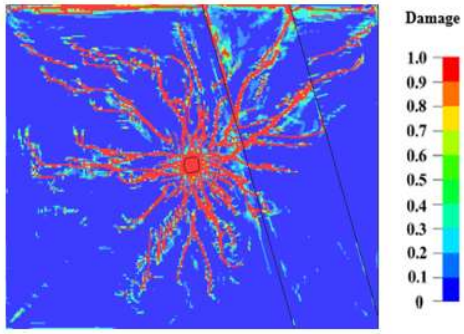

Figure 9: Scenario 2 Analysis.

a. Stress wave reflection and enhancement on the first and second interfaces

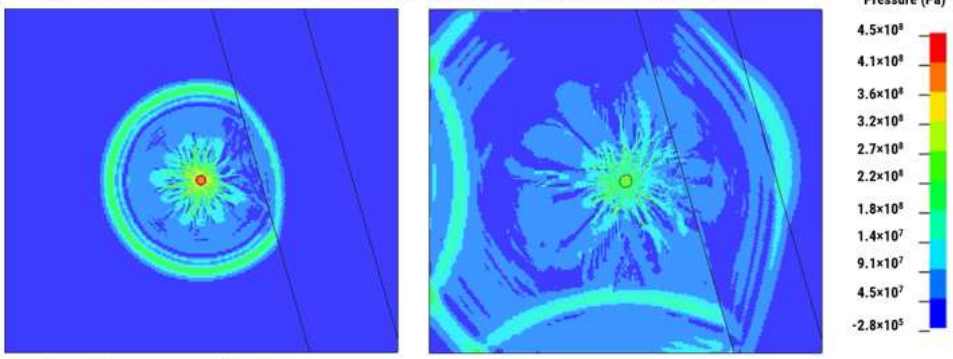

b. Stress wave reflection

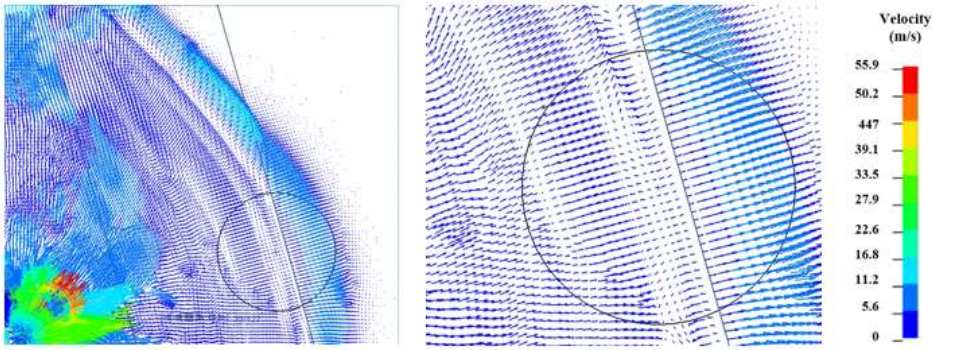

Figure 10: Stress wave distribution across the fault.

4.3. Scenario 3-Quartz Vein with Intersecting Joints

The third scenario presents fragmentation across the quartz vein intersected by the joints. The layout of the scenario, fragmentation image, and fragmentation analysis are presented in Figure 11(a) to (d). The reconstruction of the scenario in a numerical model is shown in Figure 11(e). From the fragmentation image and the simulation damage plot, the fines and good fragmentation are formed from the wave reflection on the first joint interface and good fragmentation of the quartz vein. Bigger fragments are formed between the joints from increased confinement and on the opposite side of the second joint since most of the energy is reflected or used up in multiple joint deformations [1].

Quartz material offers good stress wave transmission (Figure 12(a)) due to its hardness and stiffness and since it is brittle, it fractures easily. It should also be noted that when the stress wave meets the joint perpendicularly, depending on its intensity, fractures have a good chance to propagate to the other side of the joint (Figure 11(e) and Figure 12(a) to (c)). Comparing the rock mass to the quartz vein, the stress wave is enhanced more by crossing from the joint to the quartz vein (due to increased impedance difference) than the rock mass, increasing fracturing on the upper right corner, as seen in Figure 11(e).

a. Field mapping and survey

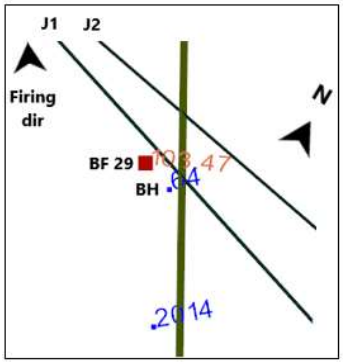

b. Vein and joints properties

Structure	Qz vein	J1	J2
Dip (°)	60	77	60
Dip/strike direction (°)	30/ 120	167/ 257	160/ 250
Width (cm)	20	5	6
Infill	Qz	clay	clay
Firing direction	West		

c. Fragmentation image

d. Fragmentation analysis

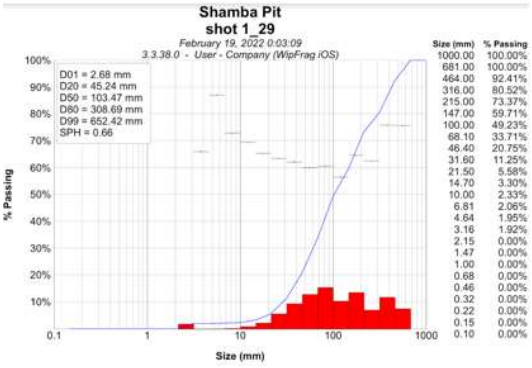

e. Scenario 3 simulation in 2D

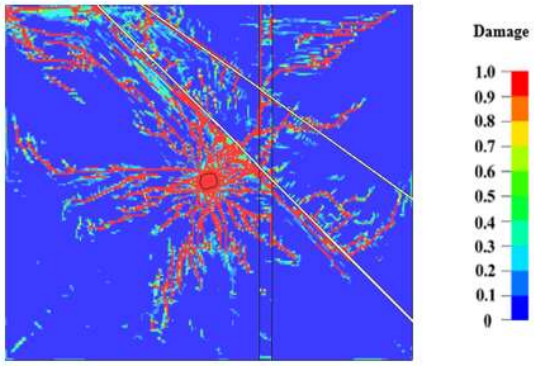

Figure 11: Scenario 4 Analysis.

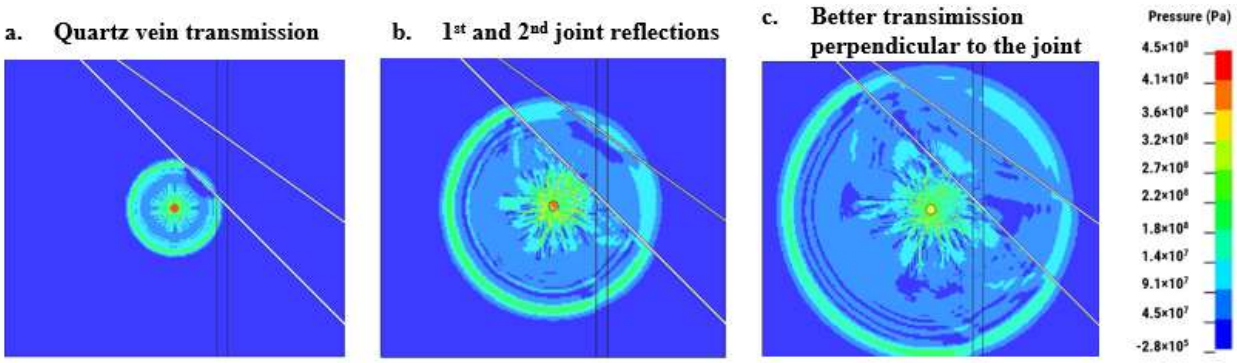

Figure 12: Stress wave propagation through a quartz vein and joints.

4.4. Scenario 4-Joints Intersecting Behind the Blasthole

The third scenario analyses the influence of joints on the pit wall formation. Mapped structures and surveyed actual toe line of shot 1 are shown in Figure 13. Comparison of the design to the actual toe line in Figure 14(a) shows under break, specifically mid-shot where joints intersect behind the perimeter blastholes. The zoomed image of the analyzed scenario and the joint properties are presented in Figure 14(b). A numerical model is created to simulate this scenario, and the results are shown in Figure 14(d) and (e).

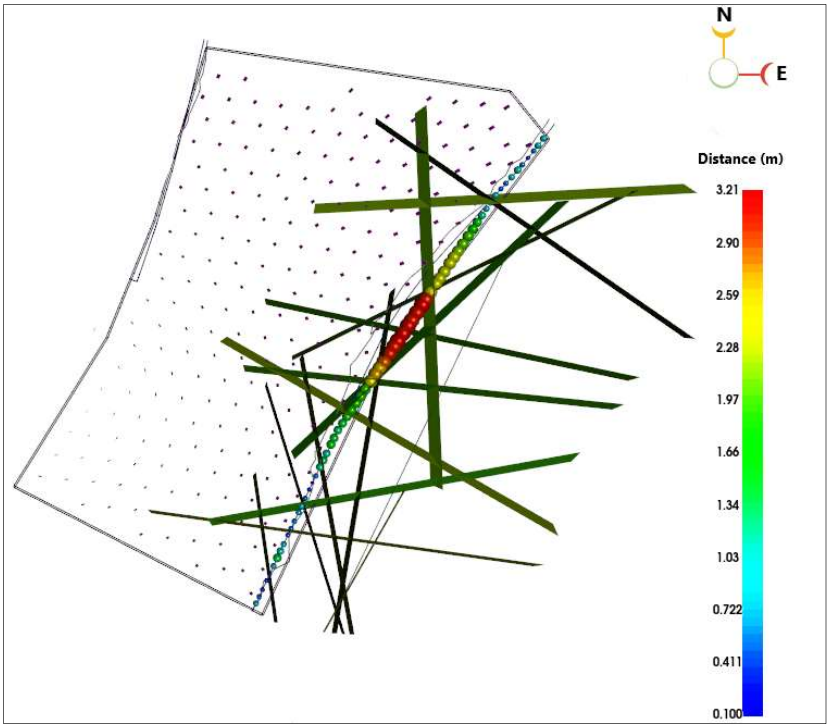

Figure 13: Structure distribution and toe formation on shot 1.

The analysis shows that the joints behind the blasthole reflect most of the stress wave unless they intersect at 90 degrees angle or close to 90 degrees. The absence of a free face hinders fracturing from reflected waves. Since the confinement increases as the wave travels toward the wall, an attenuated stress wave does not cause any fracturing. When crossing multiple joints, the stress wave is attenuated rapidly, leaving the area behind the blasthole uninterrupted while increasing fracture extents on the opposite side of the intersection.

Comparing this case to the analysis in scenario 1 (Figure 7e), when the joints intersect on the free face side, the energy gets thrown back towards the wall; this can result in pit wall/toe line over break, as seen in the bottom of Figure 13. To achieve uniform pit wall formation, pre-split is recommended to allow stress waves to reflect and cause minimum damage to the pit wall while initiating spalling to assist in fracturing the rock on the opposite side of the joints.

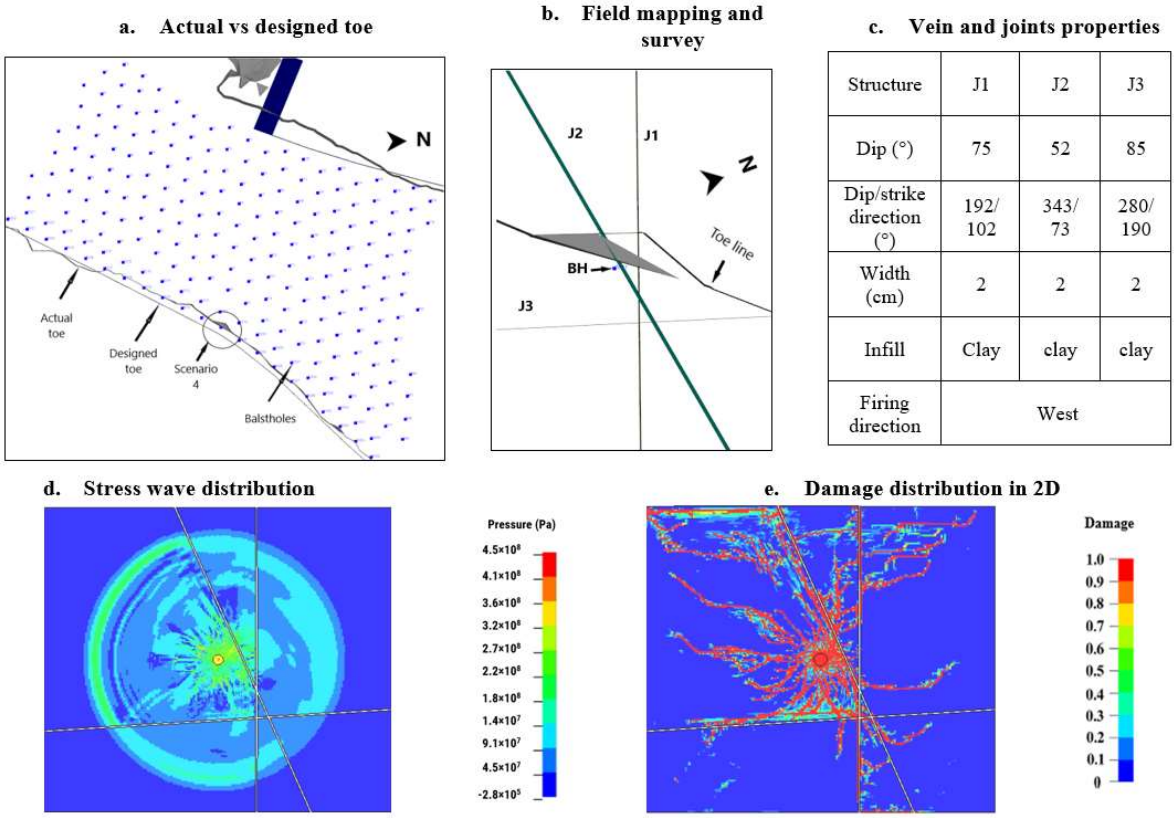

Structure	J1	J2	J3
Dip (°)	75	52	85
Dip/strike direction (°)	192/ 102	343/ 73	280/ 190
Width (cm)	2	2	2
Infill	Clay	clay	clay
Firing direction	West		

Figure 14: Scenario 4 Analysis.

5. Conclusion

This study is focused on analyzing the influence of structural features on the blast outcomes mainly the fragmentation size and the distribution and the formation of the pit wall. The analysis shows that the properties and position of the structure relative to the blasthole influence fragmentation and pit wall formation.

When the structure material is weaker and less stiff than the rock mass, the energy is reflected, causing higher damage on the incident side and oversized or uninterrupted rock mass on the opposite side of the structure. Conversely, when the structure is stronger and stiffer than the rock mass, it transfers most of the stress wave energy, and since it is brittle, it fractures easily, adding the finer fragmentation. When less stiff/weaker structures cross stiffer/stronger structures, the same concept applies to the transmission or reflection of the stress wave. Design modification can be necessary in a jointed rock mass to ensure uniform distribution of explosive energy between the reflecting joints.

The joints' positions and points of intersection relative to the free face, the blasthole, and the pit wall influence the fragmentation size and distribution across the bench and the formation of the pit wall. Joints crossing (intersecting) in front of the blasthole have the potential to cause a pit wall overbreak, while the ones crossing (intersecting) behind the blasthole cause a pit wall underbreak. Pre-split blasting is recommended to redirect explosive energy and achieve a pit design.

6. References

[1] Dotto, M.S., D., Apel, and Y., Pourrahimian, *Investigating the influence of discontinuity parameters on blast-induced fragmentation*. International Journal of Mining, Reclamation and Environment, 2024. pp. 1-25. https://doi.org/10.1080/17480930.2024.2347128

[2] Dotto, M.S., and Y., Pourrahimian, *The influence of explosive and rock mass properties on blast damage in a single-hole blasting*. Mining, 2024. **4**(1), pp. 168-188.

[3] Hustrulid, W.A., Blasting Principles for Open Pit Mining. 1999. CRC Press.

[4] Esen, S., I., Onederra, and H.A., Bilgin, *Modelling the size of the crushed zone around a blasthole*. International Journal of Rock Mechanics and Mining Sciences, 2003. **40**(4), pp. 485-495. https://doi.org/10.1016/S1365-1609(03)00018-2

[5] Ding, X., Y., Yang, W., Zhou, W., An, J., Li, and M. Ebelia, *The law of blast stress wave propagation and fracture development in soft and hard composite rock.* Scientific Reports, 2022. **12**(1), p. 17120. https://doi.org/10.1038/s41598-022-22109-z

[6] Zhang, Z.X., Rock Fracture and Blasting: Theory and Applications. 2016. Amsterdam: Elsevier.

[7] Fan, L.F., L.J., Wang, and Z.J., Wu, *Wave transmission across linearly jointed complex rock masses.* International Journal of Rock Mechanics and Mining Sciences*, 2018.* **112**, pp. 193-200. https://doi.org/10.1016/j.ijrmms.2018.09.004

[8] Huo, X., Y., Jiang, W., Wei, X., Qiu, Z., Yu, J., Nong, and Q., Li, *Three-dimensional finite element simulation and reconstruction of jointed rock masses for bench blasting.* Simulation Modelling Practice and Theory, *2024.* **135**, p. 102975. https://doi.org/10.1016/j.simpat.2024.102975

[9] Jiang, X., Y., Xue, F., Kong, H., Gong, Y., Fu, and W., Zhang, *Dynamic responses and damage mechanism of rock with discontinuity subjected to confining stresses and blasting loads.* International Journal of Impact Engineering, *2023.* **172**, p. 104404. https://doi.org/10.1016/j.ijimpeng.2022.104404

[10] Chen, S.G., and J., Zhao, *A study of UDEC modelling for blast wave propagation in jointed rock masses.* International Journal of Rock Mechanics and Mining Sciences, *1998.* **35**(1), pp. 93-99. https://doi.org/10.1016/S0148-9062(97)00322-7

[11] Ismail, M.A., and J.S., Gozon, *Effects of discontinuities on fragmentation by blasting.* International Journal of Surface Mining, Reclamation and Environment, 1987. **1**(1), pp. 21-25. https://doi.org/10.1080/09208118708944098

[12] Hanekom, J., S., Khan, and T., Hlongwane, Feasibility Stage Geotechnical Report for the Bauhinia Creek And Luika Underground Mining. 2003. Shanta Gold.

[13] Wang, Z., Y., Huang, and F., Xiong, *Three-Dimensional Numerical Analysis of Blast-Induced Damage Characteristics of the Intact and Jointed Rockmass.* Computers, Materials \& Continua, 2019. **60**(3), pp. 1189 -1206.

[14] Jayasinghe, L.B., J., Shang, Z., Zhao*, and A.T.C., Goh, Numerical investigation into the blasting-induced damage characteristics of rocks considering the role of in-situ stresses and discontinuity persistence.* Computers and Geotechnics, *2019.* **116**, p. 103207. https://doi.org/10.1016/j.compgeo.2019.103207

[15] Wei, W., X., Huo, X., Qiu, Z., Yu, J., Nong, and Q., Li, *Three-dimensional Finite Element Simulation and Reconstruction of Jointed Rock Masses for Bench Blasting.* Simulation Modelling Practice and Theory, 2024. p. 102975. https://doi.org/10.1016/j.simpat.2024.102975

[16] Borrvall, T., and W., Riedel, *The RHT concrete model in LS-DYNA*, in *8th European LS-DYNA Users Conference*. 2011.

[17] Livermore Software Technology Corporation, L., LS-DYNA Keyword User's Manual R11 Volume II Material Models. 2018.

[18] Xie, L.X.,W.B., Lu, Q.B., Zhang, Q.H., Jiang, M., Chen, and J., Zhao, *Analysis of damage mechanisms and optimization of cut blasting design under high in-situ stresses.* Tunnelling and Underground Space Technology, 2017. **66**, pp. 19-33. https://doi.org/10.1016/j.tust.2017.03.009

[19] Dehghan Banadaki, M.M., and B., Mohanty, *Numerical simulation of stress wave induced fractures in rock.* International Journal of Impact Engineering, 2012. **40-41**, pp. 16-25. https://doi.org/10.1016/j.ijimpeng.2011.08.010

[20] Hansson, H., Determination of Properties for Emulsion Explosives Using Cylinder Expansion Tests and Numerical Simulation. 2009. Stockholm and Luleå.

[21] Dotto, M., Y., Pourrahimian, T., Joseph, and D., Apel, *Assessment of blast energy usage and induced rock damage in hard rock surface mines.* CIM Journal, 2022. **13**(4), pp. 166-180. https://doi.org/10.1080/19236026.2022.2126924

[22] Forsyth, W.W., *A discussion of blast-induced overbreak in underground excavations,* in *International Symposium On Rock Fragmentation By Blasting.* 1993. pp. 161-166.

[23] WipWare. Sampling and Analysis Guide. 2021.